Theoret. Comput. Fluid Dynamics (2004)
Digital Object Identifier (DOI) 10.1007/s00162-004-0131-7

Theoretical and Computational Fluid Dynamics

Original article

From global to local bifurcations in a forced Taylor–Couette flow

V. Iranzo[1], F. Marques[1], J.M. Lopez[2]

[1] Department of Applied Physics, U. Politècnica de Catalunya, Jordi Girona Salgado s/n, Campus Nord B5, 08034 Barcelona, Spain
[2] Department of Mathematics and Statistics, Arizona State University, Tempe, AZ 85287, USA

Received October 13, 2003 / Accepted May 25, 2004
Published online September 1, 2004
Communicated by H.J.S. Fernando

Abstract. The unfolding due to imperfections of a gluing bifurcation occurring in a periodically forced Taylor–Couette system is analyzed numerically. In the absence of imperfections, a temporal glide-reflection Z_2 symmetry exists, and two global bifurcations occur within a small region of parameter space: a heteroclinic bifurcation between two saddle two-tori and a gluing bifurcation of three-tori. As the imperfection parameter increase, these two global bifurcations collide, and all the global bifurcations become local (fold and Hopf bifurcations). This severely restricts the range of validity of the theoretical picture in the neighborhood of the gluing bifurcation considered, and has significant implications for the interpretation of experimental results.

Key words: Taylor–Couette flow, periodic forcing, symmetry breaking, gluing bifurcation
PACS: 47.20.Ky, 47.20.Lz, 47.20.Ft

1 Introduction

Most natural systems contain more than two frequencies, and the behavior of systems with three frequencies is still not well understood; it is not even known whether there are universal three-frequency behaviors (Glazier and Libchaber [14]). However, to date, known examples of three-tori ($\mathbb{T}^3$) in Navier–Stokes type systems are scarce, and most of them have been reported for studies where the equations have been discretized spectrally and only a small number of modes were retained (Franceschini [10]; Giberti and Zanasi [13]).

The results presented here are of $\mathbb{T}^3$ solutions from a numerical computation of the Navier–Stokes equations with no-slip boundary conditions, restricted to an axisymmetric subspace. The system is periodically forced, and has a discrete (Z_2) space-time symmetry. The $\mathbb{T}^3$ solutions for the symmetric system where reported in Lopez and Marques [18]. The $\mathbb{T}^3$ exhibit a rich dynamics including two global bifurcations, a heteroclinic cycle and a gluing bifurcation.

Global bifurcations play a key role as organizing centers in fluid dynamics, especially where multiple states co-exist. Their systematic study has generally been limited to theoretical analysis of normal forms

Correspondence to: J.M. Lopez (e-mail: lopez@math.asu.edu)

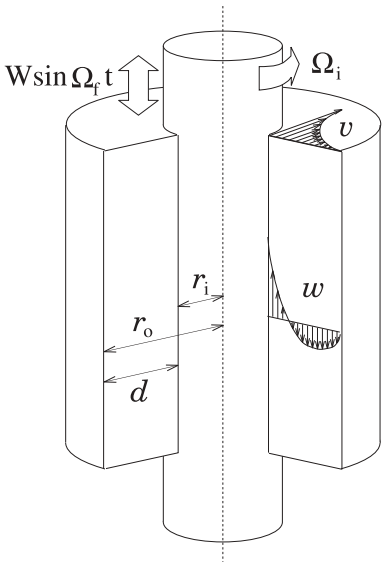

Fig. 1. Schematic of the flow configuration

and other low-dimensional canonical models, and to experimental investigations. A class of global bifurcations that has been receiving much attention of late is the gluing bifurcation (Cox [8]; Armbruster et al. [5]; Abshagen et al. [2]). This is a global bifurcation where two symmetrically related time-periodic states simultaneously become homoclinic to an unstable saddle state and result in a single symmetric time-periodic state, as a parameter is varied.

Although symmetric systems are very important and have particularly interesting dynamics (Golubitsky et al. [16]; Chossat and Lauterbach [7]), they are idealizations. Any real system is not exactly symmetric, due to the presence of unavoidable imperfections, however small. This raises the problem of the effect of the imperfections on the dynamics of a symmetric system. The effects of very small imperfections on the gluing bifurcation in the temporally forced Taylor–Couette flow was analyzed in Marques et al. [22], where good agreement with the theoretical analysis of the unfolding of the gluing bifurcation was found for very small values of the imperfection parameter. In this paper, we analyze the drastic changes that the 3-tori branches undergo when the magnitude of the imperfection is increased.

The model problem we consider is the flow between two coaxial finite cylinders (see Fig. 1) with stationary top and bottom end-walls and outer cylinder. The inner cylinder rotates at constant angular velocity Ω_i and oscillates in the axial direction with velocity $W\sin(\Omega_f t)$, where Ω_i, Ω_f, and W are dimensional parameters. Its radius is r_i, the radius of the outer cylinder is r_o, their length is L and the annular gap between the cylinders is $d = r_o - r_i$. The nondimensional governing parameters are:

the radius ratio	$e = r_i/r_o$,
the length-to-gap ratio	$\Lambda = L/d$,
the Couette flow Reynolds number	$Ri = dr_i\Omega_i/\nu$,
the axial Reynolds number	$Ra = Wd/\nu$,
and the nondimensional forcing frequency	$\omega_f = d^2\Omega_f/\nu$.

From now on, all variables and parameters are rendered non-dimensional, using the gap d and the viscous time d^2/ν as units for space and time respectively. The basic flow is time-periodic with period $T_f = 2\pi/\omega_f$, synchronous with the forcing and independent of the azimuthal coordinate. The incompressible Navier–Stokes equations governing this problem are invariant to rotations about the common axis, $SO(2)$, and a temporal glide-reflection Z_2. This Z_2 group is generated by the discrete symmetry S that is a reflection orthogonal to the axis with a simultaneous time translation of a half forcing period and satisfies $S^2 = I$. The groups $SO(2)$ and Z_2 commute for this problem. The equations are solved in an axisymmetric subspace invariant to $SO(2)$, and so the only relevant symmetry group is Z_2.

Recent experimental investigations of unforced Taylor–Couette flow in annuli with length-to-gap ratios Λ of order 10 have identified stable $\mathbb{T}^3$ solutions and Shil'nikov-type dynamics (Abshagen et al. [1]), and also the presence of an imperfect gluing bifurcation (von Stamm et al. [27]; Abshagen et al. [2]). Analysis of the experimental results indicate that the dynamics associated with the gluing bifurcation take place in an axisymmetric ($SO(2)$ invariant) subspace, even though the observations of these dynamics are from solutions with broken $SO(2)$ symmetry. We have also found a gluing bifurcation in computed solutions of the temporally forced Taylor–Couette system with $\Lambda = 10$ (Lopez and Marques [18]; Marques et al. [23]; Marques et al. [22]). It is very difficult to drive a pure sinusoidal oscillation in an experiment, and since for deviations from sinusoidal oscillations S ceases to be a symmetry group of the system, an imperfection of the sinusoidal forcing is considered here. The spatio-temporal glide reflection symmetry can be broken in a very controlled and simple manner, by adding a small multiple of the first temporal harmonic of the forcing. The axial oscillations are given by the expression $W[\sin(\Omega_f t) + \epsilon \sin(2\Omega_f t)]$, where ϵ is a measure of the imperfection.

The axisymmetric Navier–Stokes equations have been solved with the spectral-projection method described in Marques et al. [23] and Lopez et al. [20], using 80 axial and 64 radial modes, and a time-step $\delta t = T_f/200$. The boundary conditions where the endwalls meet the moving inner cylinder are discontinuous, and an accurate numerical treatment that mimics the experimental conditions has been used to deal with this discontinuity (see Lopez and Shen [21] for details). Here, we only consider variations in Ri and ϵ, keeping all other parameters fixed ($\Lambda = 10$, $e = 0.905$, $Ra = 80$, $\omega_f = 30$). The identification of the $\mathbb{T}^3$ solutions was significantly helped by the use of a global Poincaré map for the system (i.e., strobing at the forcing frequency ω_f).

The spectral convergence of the code was carefully analyzed in Lopez and Shen [21]; for Ri values one order of magnitude larger ($Ri = 3000$) than the ones used in this study ($Ri \sim 280$), and with the same resolution (80×64 modes) the velocity field converges to five figures ($1 : 10^5$). Some of the dynamical changes reported in this paper take place in a very small Ri range; increasing the resolution (the number of modes) produces a small shift in Ri, without altering the nature of the reported bifurcations. This same behavior has been reported in a similar problem (Lopez et al. [19]).

2 The symmetric system, $\epsilon = 0$

The analysis of the dynamics when the space-time symmetry is not broken ($\epsilon = 0$) was studied in Marques et al. [23]. A one-dimensional route in parameter space was analyzed, by increasing the Reynolds number Ri. The system undergoes a sequence of local and global bifurcations and becomes chaotic. This route to chaos involves a new and convoluted symmetry breaking, including heteroclinic, homoclinic, and gluing bifurcations of $\mathbb{T}^3$.

An overall description of our one-dimensional path is schematically presented in Fig. 2. The solid curves correspond to stable $\mathbb{T}$, $\mathbb{T}^2$, and $\mathbb{T}^3$ solution branches which were encountered. The dashed curves connecting them, corresponding to unstable solution branches, are only plausible conjectures. The unstable solutions have been computed numerically only very close to the homoclinic and heteroclinic bifurcation processes, and the conjectured connections are based on some of the physical properties of the corresponding flows (Marques et al. [23]). The primary branch consists of S-invariant tori. The basic state, due to the periodic forcing, is a limit cycle T_p^1 that undergoes a supercritical Neimark–Sacker bifurcation to a two-torus, T_p^2, at the point labeled NS. This is the generic scenario of a Z_2-symmetric Neimark–Sacker (Kuznetsov [17]). The resulting $\mathbb{T}^2$ is S-invariant, but obviously the solutions (trajectories) on it are not S-invariant by virtue of the fact that the two frequencies on the $\mathbb{T}^2$ are incommensurate. This $\mathbb{T}^2$ loses stability, but remains S-invariant as Ri is increased, and solution trajectories evolve towards a $\mathbb{T}^3$.

The $\mathbb{T}^3$ branch that exists and is stable in the range $Ri \in [A, C]$ in Fig. 2 is born at a heteroclinic bifurcation with two S-symmetrically related unstable $\mathbb{T}^2$, at point A in the figure. At this same point A, T_p^2 becomes unstable. The emerging three-tori, T_p^3, is S-invariant. With an increasing Ri, T_p^3 becomes homoclinic to the unstable $\mathbb{T}^2$ from the primary branch (T_p^2) at point B. At this homoclinic point, the $\mathbb{T}^3$ suffers a symmetry-breaking reverse gluing bifurcation and splits into two non-symmetric $\mathbb{T}^3$, T_t^3 and T_b^3, that are symmetrically related (S transforms one into the other).

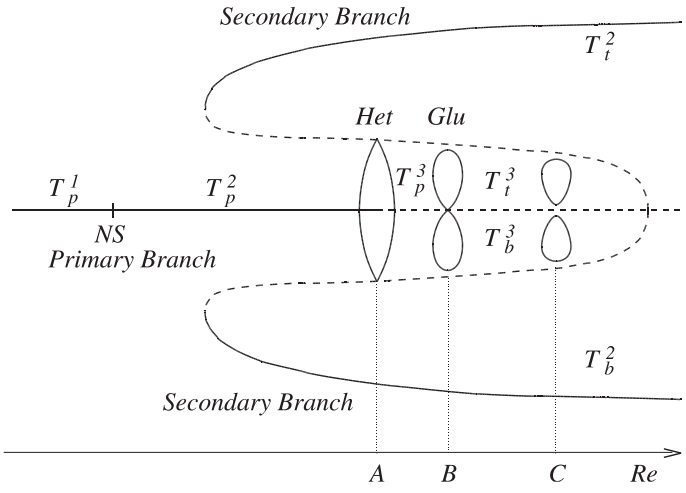

Fig. 2. Bifurcation diagram for the $\epsilon = 0$ case, showing the primary, secondary and $\mathbb{T}^3$ branches; the solid (dashed) lines are the stable (unstable) branches

Over the range of *Ri* where three-tori solutions exist, the second frequency associated with the $\mathbb{T}^2$ solutions is almost constant, $\omega_s = 5.2 \pm 3\%$. In contrast, the third frequency associated with the $\mathbb{T}^3$, ω_{VLF}, is very small, and the corresponding period $T_{\mathrm{VLF}} = 2\pi/\omega_{\mathrm{VLF}}$ experiences dramatic changes over this parameter range, as shown in Fig. 3a. This figure shows the two *Ri* values where T_{VLF} becomes unbounded, corresponding to the heteroclinic bifurcation at *A* and the gluing bifurcation at *B*. The $\mathbb{T}^3$ bifurcations are schematically shown in Fig. 3b. For ease of discussion, we represent $\mathbb{T}^3$ as limit cycles and $\mathbb{T}^2$ as fixed points. This analogy works since the two suppressed frequencies, ω_f and ω_s, are almost constant over the range of interest in *Ri* (in fact, ω_f is constant), and they do not play an essential role in the dynamics near the bifurcation points of the $\mathbb{T}^3$. The gluing bifurcation is the only symmetry breaking bifurcation we have observed in this system. The importance of the Z_2 symmetry in the Taylor–Couette problem, and its association with complex dynamics (e.g., homoclinic and Shil'nikov bifurcations) was pointed out by Mullin and Cliffe [25], and was also reviewed in Mullin [24].

Increasing *Ri* beyond a critical value (point *C* in Fig. 2), the $\mathbb{T}^3$ branch cannot be continued further and the flow evolves to a $\mathbb{T}^2$ that is not *S*-invariant. In fact, there are two such $\mathbb{T}^2$ branches, symmetrically related, termed *secondary branch* in Fig. 2. Along these secondary branches, a standard (i.e., not influenced by symmetries) route to chaos via quasi-periodicity, with lockings in resonance horns and torus break-ups, is observed. These secondary $\mathbb{T}^2$ branches are robust, i.e., they exist for a much larger range in *Ri* than the $\mathbb{T}^3$ branches.

The second frequency of the $\mathbb{T}^2$ solutions is associated with an unsteady coupling between the endwall vortices and the jets emanating from the boundary layer on the inner cylinder, and manifests itself in the form

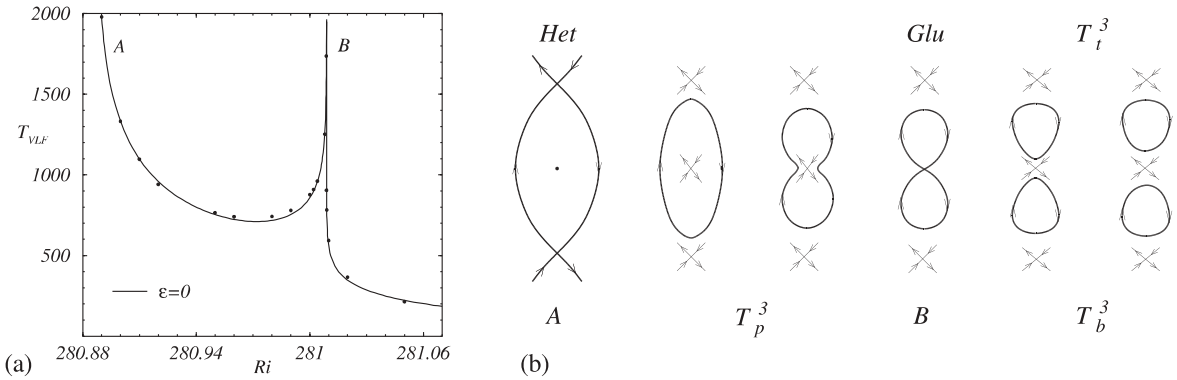

Fig. 3. (**a**) Variation of $T_{\mathrm{VLF}} = 2\pi/\omega_{\mathrm{VLF}}$ with *Ri* for $\epsilon = 0$. Symbols correspond to computed cases and lines are logarithmic fits. (**b**) Schematic of the bifurcation sequence for the $\mathbb{T}^3$ solutions depicted in a). In this schematic, $\mathbb{T}^2$ are represented as fixed points and $\mathbb{T}^3$ as cycles

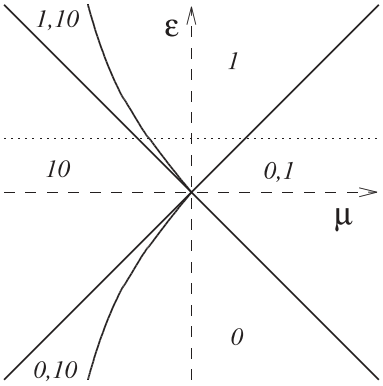

Fig. 4. Bifurcation diagram for the unfolding of the gluing bifurcation

of modulations located close to either the top or bottom endwall. These modulated stable secondary branches are accordingly named T_t^2 and T_b^2. The symmetric $\mathbb{T}^2$ on the primary branch (T_p^2) has modulations near both endwalls, as do the other various unstable $\mathbb{T}^2$, the difference between these is in the relative phase between the oscillations at both endwalls. The details of these flows can be found in Marques et al. [23].

The three $\mathbb{T}^2$ to which the $\mathbb{T}^3$ are either heteroclinically or homoclinically asymptotic are the organizing centers for the dynamics of the $\mathbb{T}^3$. In fact, the $\mathbb{T}^3$ flows are essentially slow drifts, with very low frequency (VLF), between the unstable $\mathbb{T}^2$. Similar very low frequency states have also been observed experimentally (von Stamm et al. [26, 27]; Busse et al. [6]) in an unforced Taylor–Couette flow with aspect ratio of order ten, as is the aspect ratio in our computations.

3 The imperfect system for small ϵ ($< 10^{-5}$)

By varying Ri and ϵ and keeping all other parameters fixed ($\Lambda = 10$, $e = 0.905$, $Ra = 80$, $\omega_f = 30$), we now analyze the evolution and changes in the $\mathbb{T}^3$ branches due to the imperfection parameter ϵ. In particular, the gluing bifurcation (a simultaneous collision of T_t^3 and T_b^3 with an unstable symmetric $\mathbb{T}^2$) no longer exists due to the forced symmetry breaking.

A classification of possible gluing bifurcation scenarios was obtained and analyzed in Turaev [28]; Turaev and Shil'nikov [29]; Gambaudo et al. [11]. The unfolding of the bifurcation is described by two parameters, μ (related to the Reynolds number in our problem) and ϵ, the imperfection parameter. Figure 4 is a schematic of the bifurcation diagram. The horizontal axis ($\epsilon = 0$) corresponds to perfect Z_2 symmetry. For $\mu < 0$, a symmetric limit cycle labeled 10 (our T_p^3) collides with the saddle at $\mu = 0$, forming a homoclinic curve with two closed loops; for $\mu > 0$, the cycle 10 splits into two asymmetric limit cycles, labeled 0 and 1 (our T_t^3 and T_b^3 respectively), which are related by the symmetry. For $\epsilon \neq 0$, the gluing bifurcation splits into two separate single-loop homoclinic bifurcations, corresponding to the solid straight lines in Fig. 4. These lines delimit four regions. Two of them are extensions of the symmetric case and contain the single limit cycle 10 or the two limit cycles 1 and 0, which are no longer symmetrically related. In the two additional regions only one limit cycle exists, 1 and 0 respectively; but there also exist two additional narrow cusp-shaped regions, where two limit cycles coexist, 1 and 10, and 0 and 10, respectively. The three limit cycles (0, 1, and 10) involved in the gluing bifurcation in the symmetric case give rise to three branches of limit cycles that disappear in generic homoclinic bifurcations (collision of the limit cycle with a saddle) when $\epsilon \neq 0$, corresponding to the solid lines in Fig. 4, i.e.; the gluing bifurcation splits into three generic homoclinic bifurcations. The dotted line in the figure corresponds to a typical path in the presence of a fixed imperfection ($\epsilon \neq 0$).

These scenario corresponds to a gluing bifurcation of limit cycles that collide with a fixed point. When applying this description to a gluing bifurcation of $\mathbb{T}^3$, that collides with $\mathbb{T}^2$, the situation is much more complicated. The collision of $\mathbb{T}^2$ and $\mathbb{T}^3$ does not happen on a single curve; the stable and unstable manifolds of the $\mathbb{T}^2$ intersect transversally, and a homoclinic structure exists in an exponentially narrow region of parameter space. The curves in Fig. 4 become extremely narrow regions; now the gluing bifurcation, as well as the other homoclinic/heteroclinic curves, are no longer single events, but rather complex bifurcational

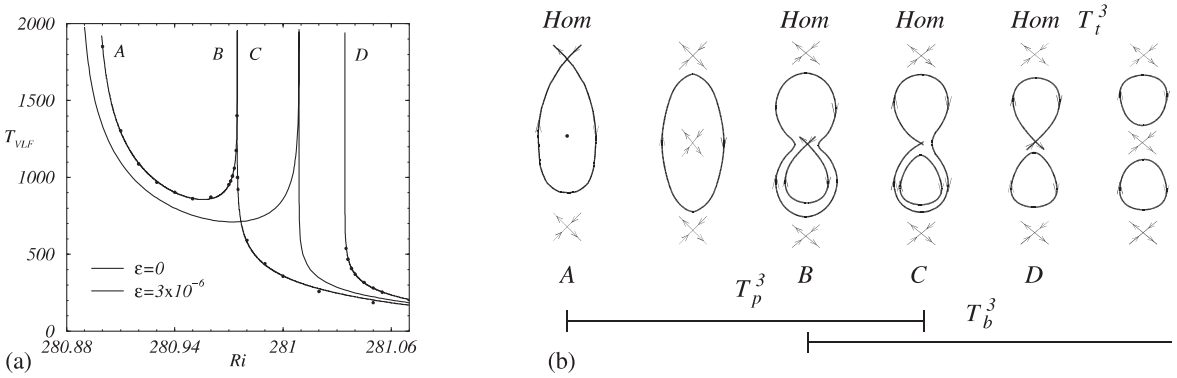

Fig. 5. (**a**) Variation of $T_{\rm VLF} = 2\pi/\omega_{\rm VLF}$ with Ri. Symbols correspond to computed cases and solid lines are logarithmic fits, for $\epsilon = 3 \times 10^{-6}$; dashed lines correspond to $\epsilon = 0$. (**b**) Schematic of the bifurcation sequence for the $\mathbb{T}^3$ solutions depicted in (**a**); in this schematic, $\mathbb{T}^2$ are represented as fixed points and $\mathbb{T}^3$ as cycles

processes. These take place in exponentially narrow regions, involving an infinite number of periodic solutions of increasing periods, Smale horseshoes and more. The complete picture is unknown. For examples, details and illustrations of very similar processes, see Kuznetsov [17] § 9.5. These considerations apply to all the homoclinic/heteroclinic bifurcations we have found, although we will continue talking of bifurcations instead of complex bifurcational processes in an exponentially narrow region, for ease of exposition.

The $\mathbb{T}^3$ solutions have three incommensurate frequencies: the forcing frequency, $\omega_f = 30$, a second frequency at $\omega_s \approx 5.2$, and a very low frequency $\omega_{\rm VLF}$ which is three orders of magnitude smaller than ω_s. We have used the period $T_{\rm VLF}$ to precisely locate the global bifurcations of the $\mathbb{T}^3$ branches. Figures 3a and 5a show the variation of $T_{\rm VLF}$ as a function of Ri for the symmetric case ($\epsilon = 0$) and one asymmetric case ($\epsilon = 3 \times 10^{-6}$), respectively. The solid curves are best fits of the form $T_{\rm VLF} \sim \lambda^{-1} \ln(1/|Ri - Ri_{crit}|) + a$, which is the asymptotic behavior of the period close to a homoclinic connection (Gaspard [12]). The logarithmic fits give the critical Ri for the infinite-period bifurcations; at $\epsilon = 0$, $Ri_{Het} = 280.88736$ and $Ri_{Glu} = 281.00885$. The factor λ is the eigenvalue corresponding to the unstable direction of the hyperbolic fixed point (saddle $\mathbb{T}^2$). The values obtained for $\epsilon = 0$ are $\lambda_{Het} = 2.43 \times 10^{-3}$ and $\lambda_{Glu} = 1.047 \times 10^{-2}$. For $\epsilon \neq 0$, the $T_{\rm VLF} \to \infty$ gluing bifurcation splits into three distinct homoclinic bifurcations as shown in Fig. 5a. Note that the range in Ri where the 1 and 10 $\mathbb{T}^3$ branches coexist (i.e., the width of the cusp region in Fig. 4) is very narrow for the imperfections considered and so the two distinct homoclinic bifurcations appear to coincide on the scale of the graphics in Fig. 5a. Specifically, for $\epsilon = 3 \times 10^{-6}$, the width in Ri of the cusp coexistence region is 2.40×10^{-4}. This behavior agrees with the theory of the unfolding of a gluing bifurcation, depicted in Fig. 4. The periods of the $\mathbb{T}^3$ follow the same asymptotic logarithmic expression as for $\epsilon = 0$, showing that the $\mathbb{T}^3$ for $\epsilon \neq 0$ disappear in a collision with a saddle $\mathbb{T}^2$ (a generic homoclinic bifurcation).

Figure 5b illustrates schematically the sequence of bifurcations on the $\mathbb{T}^3$ branches in the imperfect ($\epsilon \neq 0$) case; $\mathbb{T}^3$ are depicted as limit cycles and $\mathbb{T}^2$ as fixed points, as in Fig. 3a. Both the gluing and the heteroclinic bifurcations become standard homoclinic bifurcations, and we have three different branches, T_p^3, T_t^3 and T_b^3 (corresponding to 10, 0 and 1, respectively, in Fig. 4); these overlap for different values of Ri, in agreement with the theoretical description in Fig. 4. The equations of the straight lines and the cusp curve in Fig. 4 can be obtained from the numerical simulations. As a result, we have obtained the saddle index of the gluing bifurcation (the ratio between the real part of the leading negative eigenvalue and the positive eigenvalue λ_1), $\delta = -\text{Real}(\lambda_2)/\lambda_1 = 1.083 > 1$.

3.1 The fate of the three-tori branches

For ϵ sufficiently small, our numerical simulations produce dynamics precisely in accord with the dynamical systems theory for the unfolding of a gluing bifurcation: three different branches of $\mathbb{T}^3$ exists, and they appear in homoclinic bifurcations close to the gluing point. But this agreement is achieved only in a very small range of the imperfection parameter, i.e., for $|\epsilon| \lesssim 4.5 \times 10^{-6}$.

For the particular imperfection considered here, the branch of symmetric $\mathbb{T}^3$, labeled T_p^3, undergoes a close-by (at lower Ri) homoclinic global bifurcation, and when ϵ increases, the two homoclinic bifurca-

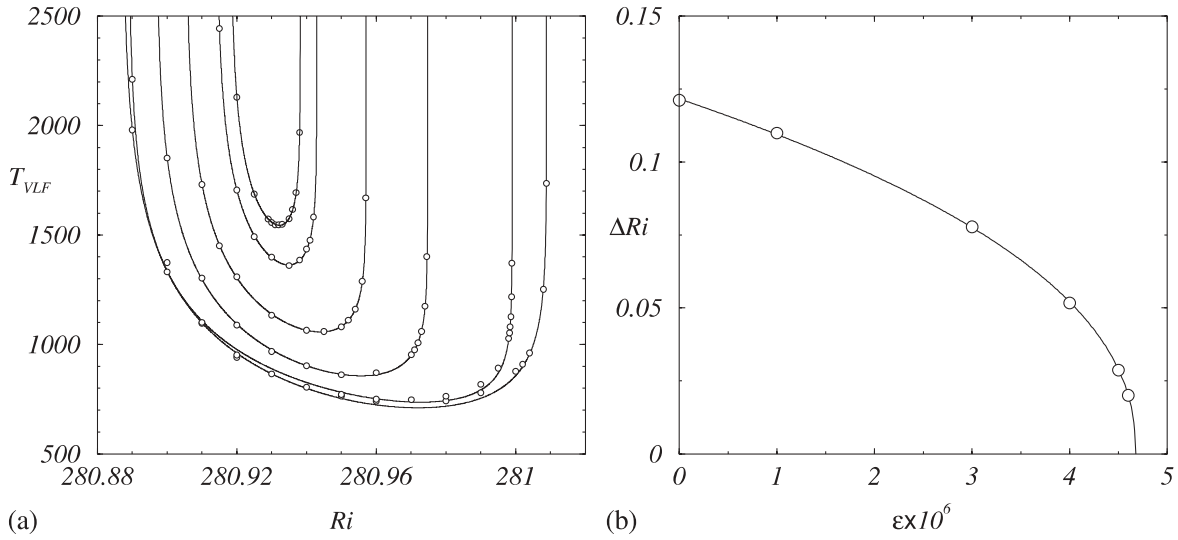

Fig. 6. (**a**) T_{VLF} of the $\mathbb{T}^3$ branch T_p^3 for different values of ϵ. (**b**) Width of the Ri range for the existence of the $\mathbb{T}^3$ branch T_p^3, as a function of ϵ

tions at either end of this branch coincide and the T_p^3 branch disappears. This collision of global bifurcations (in this case of two homoclinic bifurcations) alters the bifurcation diagram, dramatically reducing the parameter range of validity of the standard unfolding of the gluing bifurcation.

The annihilation of the T_p^3 branch is shown in Fig. 6. T_{VLF} as a function of Ri is plotted in Fig. 6a, for $\epsilon = \{0, 1, 3, 4, 4.5, 4.6\} \times 10^{-6}$. The width of the Ri range over which the T_p^3 solutions exist is plotted in Fig. 6b as a function of ϵ. This allows a precise determination of the parameter values where the T_p^3 branch disappears: $\epsilon \simeq 4.68 \times 10^{-6}$ and $Ri \simeq 280.93$

The two remaining $\mathbb{T}^3$ branches, labeled T_t^3 and T_b^3, become unstable at higher Ri. With increasing ϵ, the homoclinic bifurcation points where these branches are born move apart, one to smaller and the other to larger Ri, as shown in Fig. 5. Therefore, the parameter range of existence of the asymmetric $\mathbb{T}^3$ labeled T_t^3 shrinks until it disappears at about $\epsilon \approx 10^{-5}$.

Only one of the $\mathbb{T}^3$ branches, T_b^3, is sufficiently robust to be observable in a significant window of parameter space (for $\epsilon > 10^{-5}$). The fate of this branch is addressed in the next section. For negative ϵ values, the dynamics is exactly the same as for positive ϵ, except that *top* and *bottom* are interchanged; for example, the only $\mathbb{T}^3$ branch observable for $\epsilon < -10^{-5}$ is T_t^3. Therefore, we only need to consider the case $\epsilon > 0$.

4 New branches at larger ϵ ($\gtrsim 10^{-4}$)

For the next order of magnitude in ϵ, between 10^{-5} and 10^{-4}, there remains a single branch of $\mathbb{T}^3$, T_b^3. This branch appears at a homoclinic collision with an unstable $\mathbb{T}^2$, and becomes unstable at larger Ri, evolving towards T_b^2, and nothing new happens. For $\epsilon \gtrsim 10^{-4}$, a variety of new branches exist and new bifurcations take place involving the T_b^3 branch. The dynamics are very complicated and we present a summary of our numerical findings, focusing on the most relevant aspects of the new dynamics.

Figure 7 is a schematic bifurcation diagram showing the changes in the branches related to T_b^3, for different values of ϵ in the range $[1.0, 1.8] \times 10^{-4}$; these schematic diagrams are not drawn to scale. The branch T_t^2 has not been shown as it does not play any role in the dynamics around the T_b^3 branch. Solid (dashed) lines are stable (unstable) computed branches. When a solution becomes unstable, it evolves towards another stable solution, and we have indicated these evolutions with thin dotted lines. In the figure, F_n indicates a fold (also called saddle-node) bifurcation (with zero critical eigenvalue) of a $\mathbb{T}^n$, and H_n indicates a Hopf bifurcation (a pair of complex-conjugate purely imaginary eigenvalues) from a $\mathbb{T}^n$ to a $\mathbb{T}^{n+1}$; H_0 is the usual Hopf bifurcation, from a fixed point to a periodic solution, and H_1 is a Neimark–Sacker bifurcation, from a limit cycle to a quasiperiodic solution on a $\mathbb{T}^2$.

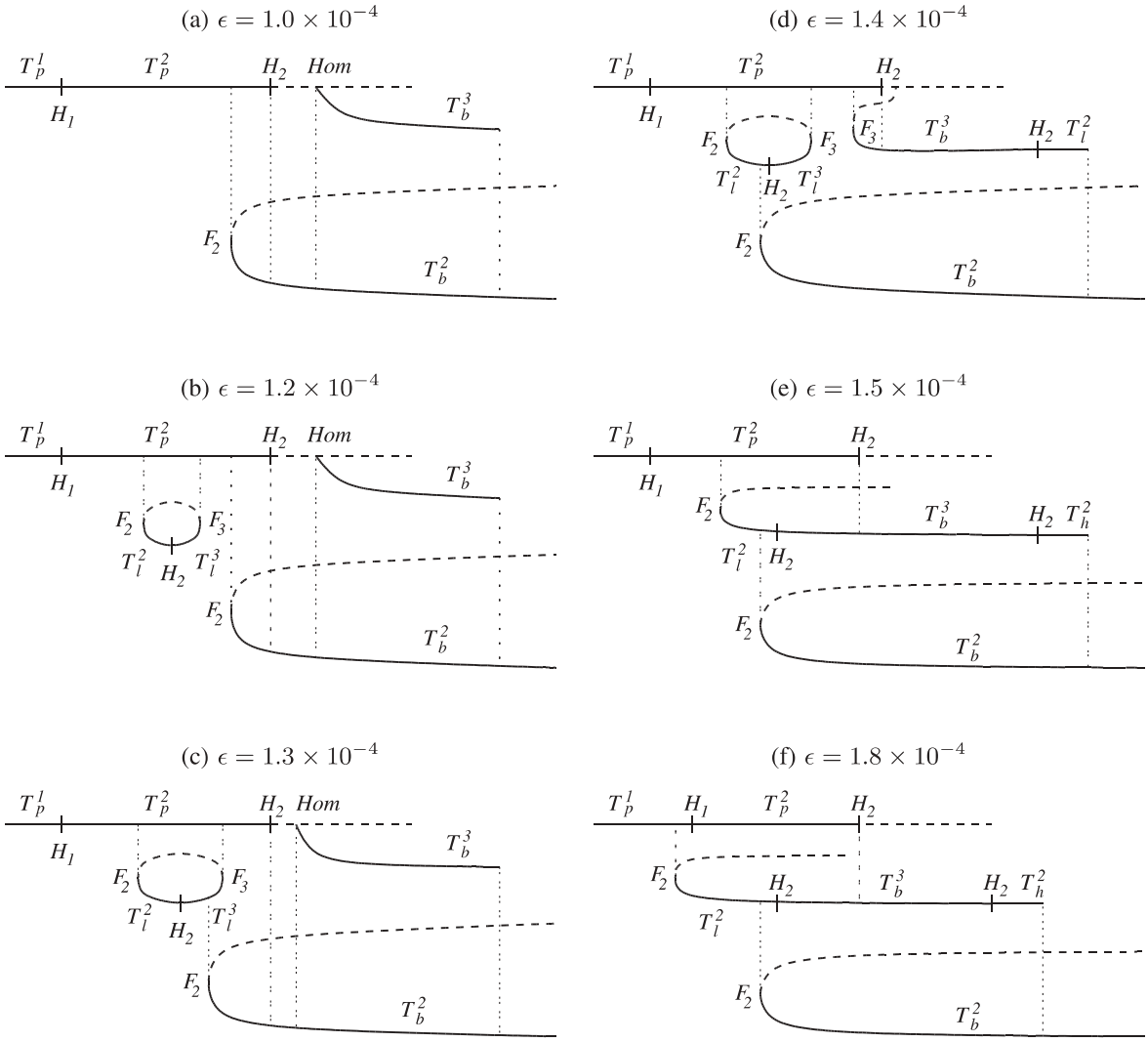

Fig. 7a–f. Schematic bifurcation diagrams (not to scale) showing the branches related to T_b^3; the solid (dashed) lines are stable (unstable) branches, and the thin dotted lines indicate the evolution of a solution when it becomes unstable

The changes displayed in Fig. 7 can be summarized as follows: at $\epsilon \lesssim 1.2 \times 10^{-4}$, an isolated solution branch appears, in a so-called isola center bifurcation (Golubitsky and Schaeffer [15]). On this branch, at *Ri* numbers *lower* than those of the T_b^3 branch, a new $\mathbb{T}^2$ (T_l^2) and a new $\mathbb{T}^3$ (T_l^3) exist. At $\epsilon \lesssim 1.4 \times 10^{-4}$, the homoclinic bifurcation at the lower end of the T_b^3 branch becomes a fold bifurcation when the T_b^3 branch develops an S-shaped profile. Moreover, at the *high-Ri* end of the T_b^3 branch, a new $\mathbb{T}^2$-branch (T_h^2) appears. At $\epsilon \lesssim 1.5 \times 10^{-4}$, the $\mathbb{T}^3$-branches T_l^3 and T_b^3 merge into a single branch (this is called a *simple bifurcation* in Golubitsky and Schaeffer [15]). Further increases in ϵ do not produce new bifurcations, and the only relevant events (up to $\epsilon \sim 3 \times 10^{-4}$) are that the T_b^3 branch shrinks, and that when T_l^2 becomes unstable, it evolves towards the T_p^1 branch instead of T_p^2. In the following subsections we describe in detail the nature and the bifurcations of the solutions just mentioned.

4.1 The isola branch: T_l^2 and T_l^3

At $\epsilon \lesssim 1.2 \times 10^{-4}$, an isolated solution branch appears, that exists in a very narrow *Ri* range; the width of the isola is $\Delta Ri = 0.012$ at $\epsilon = 1.2 \times 10^{-4}$, and grows rapidly with ϵ; $\Delta Ri = 0.029$ at $\epsilon = 1.3 \times 10^{-4}$. On this branch, at low *Ri*, there is a new $\mathbb{T}^2$, T_l^2, which is different from the other $\mathbb{T}^2$ that exists for the same parameter values, the T_p^2 on the principal branch. In Fig. 8a phase portraits of the Poincaré maps of both $\mathbb{T}^2$ are

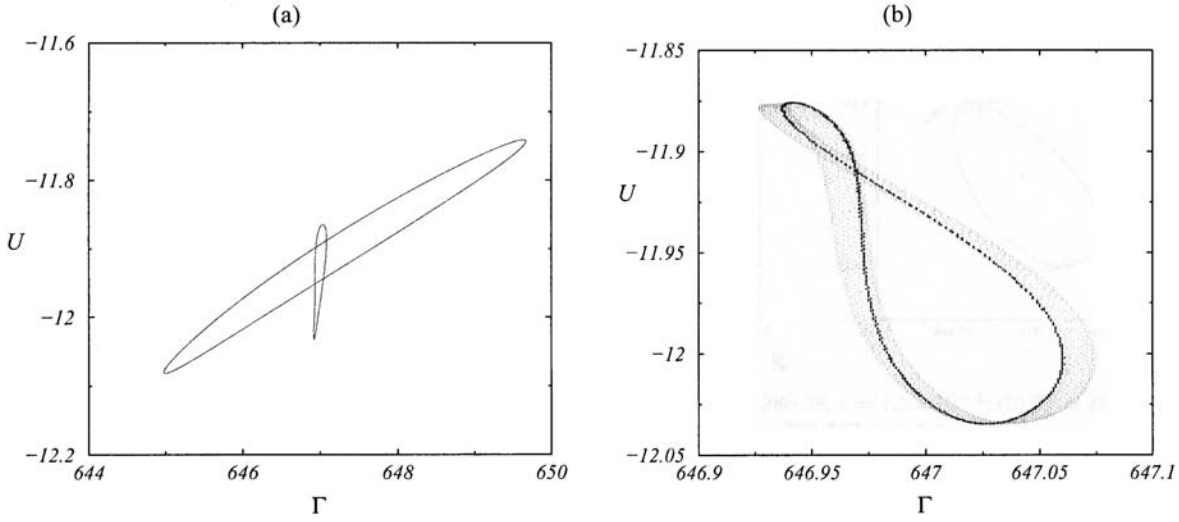

Fig. 8a,b. Phase portraits of the Poincaré map in the (Γ, U) plane, for $\epsilon = 1.3 \times 10^{-4}$, of (**a**) T_l^2 (small closed curve) and T_p^2 (large closed curve) for $Ri = 280.350$; (**b**) T_l^2 at $Ri = 280.3570$ (closed curve) and T_l^3 at $Ri = 280.3575$

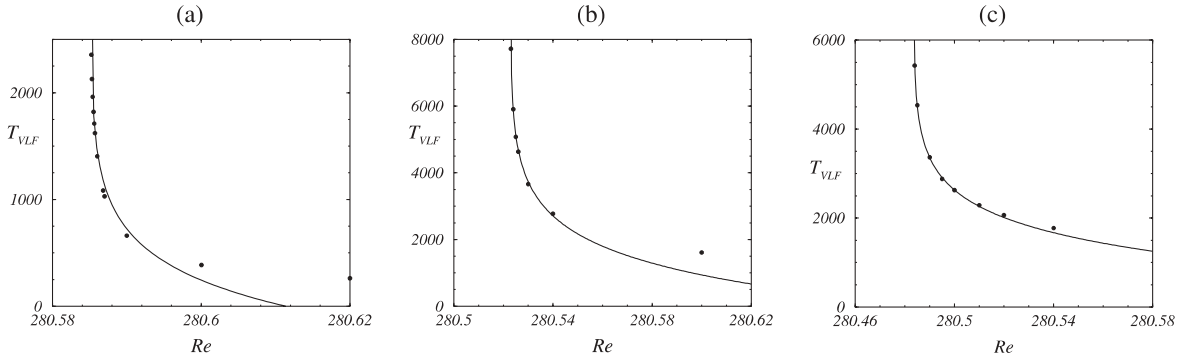

Fig. 9a–c. Variation of T_{VLF} on the T_b^3 branch with Ri, for (**a**) $\epsilon = 1.0 \times 10^{-4}$, (**b**) 1.2×10^{-4}, and (**c**) 1.3×10^{-4}. Symbols correspond to computed cases and lines are logarithmic fits

shown for the same parameter values, and they are clearly different. By increasing Ri onto the isola branch, T_l^2 undergoes a Hopf bifurcation of $\mathbb{T}^2$, H_2, leading to a $\mathbb{T}^3$-branch, T_l^3. In Fig. 8b, a T_l^2 solution and a T_l^3 solution are displayed, just before and after the H_2 bifurcation. The amplitude of the $\mathbb{T}^3$ is very small, as is expected at a supercritical Hopf bifurcation.

The phase portraits shown in Fig. 8 and in subsequent figures are the projection of the Poincaré map (time series strobed at the forcing frequency) into the plane (Γ, U), where U is the radial velocity and Γ the vertical angular momentum at a convenient Gauss–Lobato point in the annulus $(r = r_i + 0.573, z = 0.969)$.

4.2 A merging bifurcation of $\mathbb{T}^3$

For $\epsilon = \{1.0,\ 1.2,\ 1.3\} \times 10^{-4}$, the T_b^3 branch still appears at a homoclinic collision with the unstable T_p^2 branch, as evidenced in Fig. 9, showing the variation of T_{VLF} on the T_b^3 branch with Ri, with an infinite-period bifurcation. At $\epsilon \lesssim 1.4 \times 10^{-4}$, the T_b^3 branch develops an S-shaped profile, and the global homoclinic bifurcation becomes a local fold bifurcation, as shown in the schematic in Fig. 7d. Now the upper end of the T_l^3 branch and the lower end of the T_b^3 branch are fold bifurcations of $\mathbb{T}^3$, F_3. By further increasing Ri these bifurcations occur at closer values of Ri, and at $\epsilon \lesssim 1.4 \times 10^{-4}$ the T_l^3 and T_b^3 branches merge into a single branch, as shown in the schematic in Fig. 7e. In Fig. 10 are shown solutions on the T_l^3 (Fig. 10a and T_b^3 (Fig. 10b) branches, close to the respective folds F_3, for $\epsilon = 1.3 \times 10^{-4}$. The structure of the $\mathbb{T}^3$ in both branches is almost identical, differing only in size.

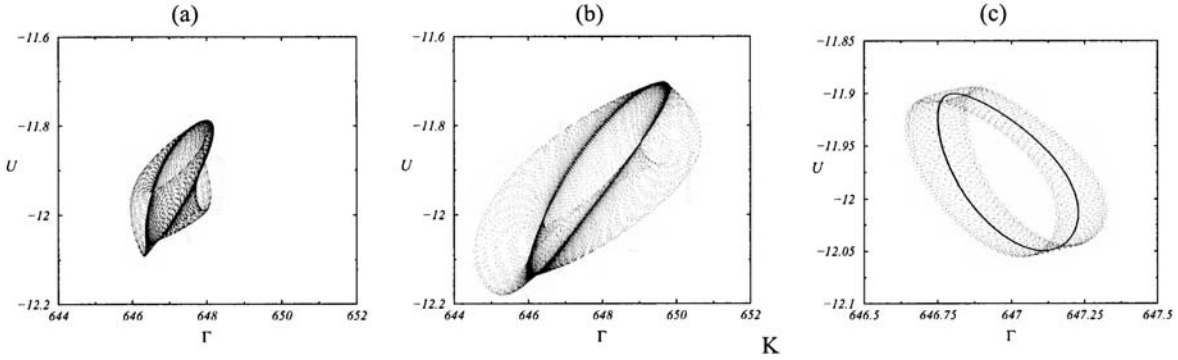

Fig. 10a–c. Phase portraits of the Poincaré map in the (Γ, U) plane of: (**a**) T_l^3 at $Ri = 280.38$, $\epsilon = 1.3 \times 10^{-4}$; (**b**) T_p^3 at $Ri = 280.48$, $\epsilon = 1.3 \times 10^{-4}$; and (**c**) T_l^2 at $Ri = 280.366$ (closed curve) and T_b^3 (torus) at $Ri = 280.367$, $\epsilon = 1.5 \times 10^{-4}$

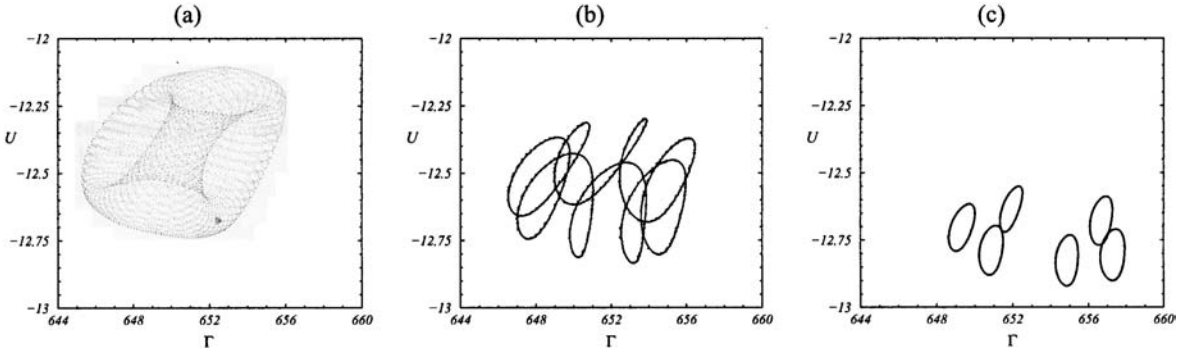

Fig. 11a–c. Phase portraits of the Poincaré map in the (Γ, U) plane of T_p^3 at $Ri = 281.100$ (torus), $Ri = 281.120$ (large closed curve) and $Ri = 281.154$ (the six small thick ovals) for $\epsilon = 1.5 \times 10^{-4}$

The branch resulting from the merging of the T_l^3 and T_b^3 branches is called T_b^3, the name of the larger (in both parameters ϵ and Ri) branch taking part in the merging. Now the T_b^3 branch at low Ri terminates at a Hopf bifurcation, H_2, on the T_l^2 branch. Fig. 10c shows a T_l^2 solution and a T_l^3 solution, just before and after the H_2 bifurcation, for $\epsilon = 1.5 \times 10^{-4}$. The amplitude of the $\mathbb{T}^3$ is very small, as is expected at a supercritical Hopf bifurcation.

4.3 A new $\mathbb{T}^2$ branch from T_b^3

For $\epsilon \gtrsim 1.3 \times 10^{-4}$, at the high-$Ri$ end of the T_b^3 branch, different lockings between the three frequencies of the $\mathbb{T}^3$ appear. Figure 11 shows three solutions at the upper end of the T_b^3 branch, for $\epsilon = 1.5 \times 10^{-4}$. The first one, at $Ri = 281.100$, has the shape of a typical Poincaré section of a $\mathbb{T}^3$. The second one, at $Ri = 281.120$, shows a $1:7$ locking between the second frequency ω_s and ω_{VLF}, which at the upper end of the T_b^3 is no longer very small, but only $1/7$ of ω_s. This value agrees with Fig. 9, showing how T_{VLF} decreases (i.e., ω_{VLF} increases) when Ri increases. The third solution depicted in Fig. 11c shows a different locking at $Ri = 281.154$, a $1:6$ locking between ω_s and the forcing frequency ω_f.

At the *high-Ri* end of the T_b^3 branch, where the frequency lockings occur, a new bifurcation appears, at $\epsilon \lesssim 1.4 \times 10^{-4}$. T_b^3 undergoes a Hopf bifurcation of $\mathbb{T}^2$, H_2, onto a $\mathbb{T}^2$-branch, T_h^2. Figure 12a shows a T_b^3 solution and a T_h^2 solution just before and after the H_2 bifurcation. The T_b^3 solution is in fact a $\mathbb{T}^2$, because we are inside the $1:6$ resonance horn between ω_s and ω_f. The amplitude of the $\mathbb{T}^3$ before the bifurcation is decreasing, as shown in Fig. 11; this is the amplitude associated with the third frequency, the former ω_{VLF}, that in the figure corresponds to the vertical thickness of the $\mathbb{T}^3$. This behavior suggests we have a supercritical Hopf bifurcation. In fact, the bifurcation is more complex, because it takes place inside or just exiting the $1:6$ resonance horn of the $\mathbb{T}^3$; nevertheless, it is clear from Figs. 11 and 12a that this amplitude collapses.

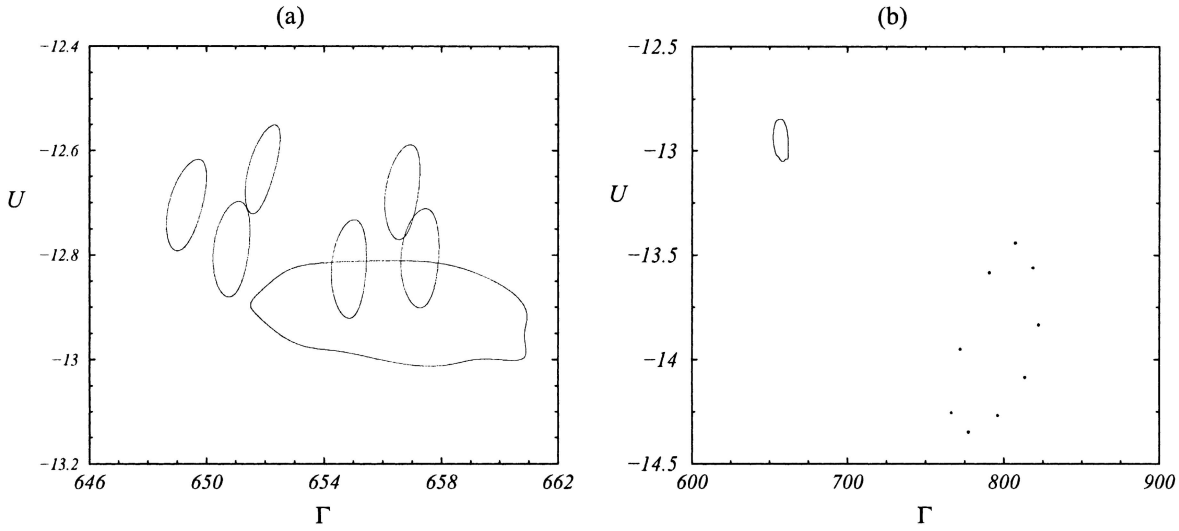

Fig. 12a,b. Phase portraits of the Poincaré map in the (Γ, U) plane of: (**a**) T_b^3 (the six ovals) at $Ri = 281.154$ and T_h^2 at $Ri = 281.155$ (large closed curve). (**b**) T_b^2 (showing a 1:9 locking) and T_h^2 (small closed curve) at $Ri = 281.16$. All solutions correspond to $\epsilon = 1.5 \times 10^{-4}$

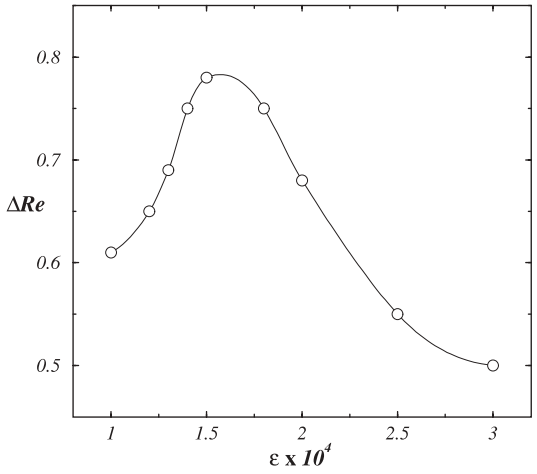

Fig. 13. Width of the Ri interval where the branch T_b^3 exists, as a function of ϵ

The new $\mathbb{T}^2$, T_h^2, is different from the other $\mathbb{T}^2$ that exists for the same parameter values on the T_b^2 branch. In Fig. 12b, both $\mathbb{T}^2$ are shown for the same parameter values and they are clearly different; in fact, the $\mathbb{T}^2$ on the T_b^2 branch shows a $1:9$ locking, while the $\mathbb{T}^2$ on the T_h^2 branch is quasiperiodic.

The T_b^3 branch, for lower ϵ values, is born in a homoclinic (global) bifurcation and becomes unstable at larger Ri through a bifurcation that we are unable to characterize. Following the new bifurcations presented in this subsection, the T_b^3 branch terminates at both ends in local Hopf bifurcations H_2, becoming a $\mathbb{T}^2$: T_l^2 and T_h^2, at the lower and higher end points of the branch, respectively. The width of the Reynolds number range, ΔRi, over which the T_b^3 branch exists is plotted as a function of ϵ in Fig. 13. There is a maximum in ΔRi, close to the value of ϵ where the T_b^3 branch merges with the T_l^3 branch, and after this merging, ΔRi decreases. We have not continued the numerical computations (as they are extremely expensive) to determine whether the T_b^3 branch disappears for some higher value of ϵ.

4.4 Torus break-up on T_b^2

The branch T_b^2, the robust bottom secondary branch shown in Fig. 2, is not connected directly via local bifurcations with the T_b^3 branch we have analyzed in detail. It only acts, as can be seen in Fig. 7, as a recipient

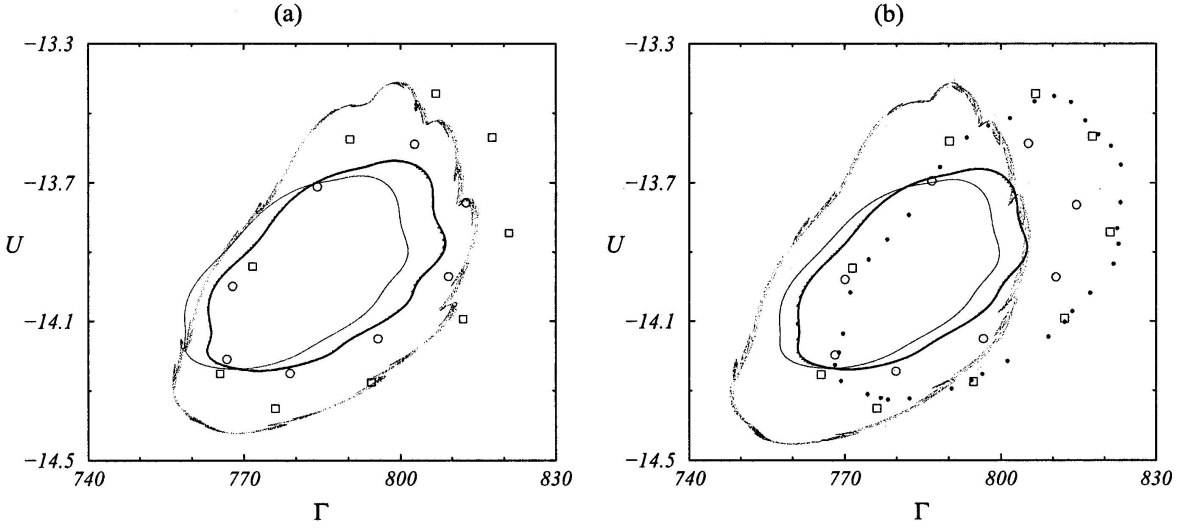

Fig. 14a,b. Phase portraits of the Poincaré map in the (Γ, U) plane of T_b^2. (**a**) $\epsilon = 1.2 \times 10^{-4}$; $Ri = 280.38$ (closed curve), $Ri = 280.40$ (thick closed curve), $Ri = 280.45$ (circles, locking 1:8), $Ri = 281.18$ (squares, locking 1:9) and $Ri = 281.80$ (torus break-up). (**b**) $\epsilon = 1.3 \times 10^{-4}$; $Ri = 280.372$ (closed curve), $Ri = 280.380$ (thick closed curve), $Ri = 280.40$ (circles, locking 1:8), $Ri = 281.0$ (small solid circles, locking 4:35), $Ri = 281.18$ (squares, locking 1:9) and $Ri = 282.2$ (torus break-up)

of the solutions on the T_b^3 branch when they become unstable at the high Ri end of the branch. When T_b^2 disappears in a fold bifurcation at low Ri, the solutions evolve towards T_b^3 (in fact, towards T_l^2 at the lower end of the $\mathbb{T}^3$ branch).

The evolution of the solutions on the T_b^2 branch in the Z_2-symmetric case ($\epsilon = 0$) was analyzed in detail in Marques et al. [23]. A typical (i.e. not influenced by symmetries, because the only symmetry of the system, S, was spontaneously broken in the gluing bifurcation) route to chaos via quasi-periodicity, locking in resonance horns, and torus break-up was reported. For $\epsilon \neq 0$, we have found the same standard scenario, differing only in minor details. As the focus of this paper is on the fate of the $\mathbb{T}^3$ branches, we do not present a detailed analysis of the T_b^2 branch. The main features are shown in Fig. 14 for two different values of ϵ, 1.2×10^{-4} and 1.3×10^{-4}. We have plotted several Poincaré sections of the $\mathbb{T}^2$, for different Ri values. At the start of the branch, where Ri is small, we have a smooth $\mathbb{T}^2$, and the solutions on it are quasiperiodic; these correspond to the smooth closed curves in the figure. Increasing Ri, several resonance horns are entered and exited, corresponding to different frequency locking ratios. Solutions with ratios 1 : 8 and 1 : 9 are shown in both figures; they are the broadest resonance horns in the parameters range considered as they have the smallest denominators. Other slender tongues corresponding to higher resonances can also be found, with increasing difficulty. Figure 14b shows a 4 : 35 locked solution, located between the resonances 1 : 8 and 1 : 9, in agreement with the Farey sequences that describe the order of appearance of the different resonance horns. By further increasing Ri, there is evidence that the $\mathbb{T}^2$ has lost smoothness, displaying the characteristic wrinkling observed, for example, in Curry and Yorke [9], and becoming a chaotic attractor at higher Ri. The Afraimovich-Shil'nikov theorem (Afraimovich et al. [3]; Anishchenko et al. [4]) describes distinct possible scenarios for the destruction of $\mathbb{T}^2$ on exiting a resonance horn.

5 Conclusions

We have analyzed in detail the dynamical consequences of the imperfections of a space-time Z_2 symmetry in a real system, Taylor–Couette flow with axial oscillations of the inner cylinder, restricted to an axisymmetric subspace. A $\mathbb{T}^3$ branch appears in the symmetric system as a result of the convoluted spontaneous symmetry breaking. For very small values of the imperfection parameter (ϵ), the dynamics agree with the theoretical scenarios, and three distinct $\mathbb{T}^3$ branches are present in the system. However, with further small increases of the imperfection parameter, two of the branches quickly disappear, leaving a single branch of $\mathbb{T}^3$, T_b^3. With further increases in ϵ, this branch undergoes drastic changes: the global homoclinic bifurcation at which it

was born becomes a local fold bifurcation, and at the two end points of the branch, Hopf bifurcations H_2 to two new $\mathbb{T}^2$ branches appear. All these complex dynamics take place in a narrow range of the imperfection parameter ($|\epsilon| \lesssim 10^{-4}$), and the range of validity of the generic unfolding of the gluing bifurcation is severely reduced.

An implication of the presence of nearby global dynamics interacting with the imperfect gluing bifurcation is that the theoretical picture of the unfolding is completely changed. So, in an experiment with even extremely small levels of imperfection, complex spatio-temporal dynamics can be present that are not obviously associated with the underlying gluing bifurcation (e.g., in our example problem, for $\epsilon \gtrsim 1.4 \times 10^{-4}$ there is only one branch of $\mathbb{T}^3$, the T_b^3 branch, that is not symmetric and does not undergo any homoclinic bifurcation at this ϵ), and their origin would be difficult to reconcile. Although the dynamical systems theory has proved to be extremely useful in providing plausible scenarios for many complex fluid problems, in some cases the range of validity of the theoretical picture in the neighborhood of a bifurcation can be extremely small, as was pointed out by Wittenberg and Holmes [30]. This is also the case in the present problem, where different complex bifurcations take place in a very small neighborhood of the gluing bifurcation, and so finding any theoretical explanation of experimental results becomes very difficult.

The dynamics we have described in this paper are interesting in their own right as they offer detailed examples of complicated local and global bifurcations of $\mathbb{T}^3$. In particular, we have found that all the global bifurcations that take place near the gluing bifurcation become local bifurcations when the imperfection parameter increases. Although the minute details of the wealth of bifurcations we have found are almost impossible to detect experimentally, some of the features can nevertheless be observed. In particular, $\mathbb{T}^3$ solutions are present in the whole parameter range we have examined. We expect, based on trends with other features in Taylor–Couette flow, that in annuli with wider gaps and smaller aspect ratios, the global bifurcations should occur over a more extensive range of Reynolds numbers. In fact, recent experimental investigations of unforced Taylor–Couette flow in annuli with height-to-gap ratios of order 10 have identified the presence of an imperfect gluing bifurcation (von Stamm et al. [27], Abshagen et al. [2]), and the analysis of the experimental results indicate that the dynamics associated with the gluing bifurcation are taking place in an axisymmetric subspace.

Acknowledgments. This work was partially supported by MCYT grant BFM2001-2350 (Spain) and NSF Grant CTS-9908599 (USA).

References

1. Abshagen, J., Pfister, G.: Low-dimensional dynamics of axisymmetric modes in wavy Taylor vortex flow. In *Physics of Rotating Fluids*, C. Egbers and G. Pfister (eds.). *Lecture Notes in Physics*, vol. 549, pp. 84–101. Springer (2000)
2. Abshagen, J., Pfister, G., Mullin, T.: Gluing bifurcations in a dynamically complicated extended flow. Phys. Rev. Lett. **87**, 224501 (2001)
3. Afraimovich, V.S., Shilnikov, L.P.: Invariant two-dimensional tori, their breakdown and stochasticity. Amer. Math. Soc. Trans. **149**, 201–212 (1991)
4. Anishchenko, V.S., Safonova, M.A., Chua, L.O.: Confirmation of the Afraimovich-Shil'nikov torus-breakdown theorem via a torus circuit. IEEE Tran. Cir. Sys. **40**, 792–800 (1993)
5. Armbruster, D., Nicolaenko, B., Smaoui, N., Chossat, P.: Symmetries and dynamics for 2-D Navier–Stokes flow. Physica D **95**, 81–93 (1996)
6. Busse, F.H., Pfister, G., Schwabe, D.: Formation of dynamical structures in axisymmetric fluid systems. In: *Evolution of Spontaneous Structures in Dissipative Continuous Systems*, F.H. Busse and S.C. Müller (eds.), *Lecture Notes in Physics*, vol. m55, pp. 86–126. Springer (1998)
7. Chossat, P., Lauterbach, R.: *Methods in Equivariant Bifurcations and Dynamical Systems*. World Scientific (2000)
8. Cox, S.M.: 2-dimensional flow of a viscous-fluid in a channel with porous walls. J. Fluid Mech. **227**, 1–33 (1991)
9. Curry, J.H., Yorke, J.A.: A transition from Hopf bifurcation to chaos: Computer experiments with maps in R^2. In: *The structure of attractors in dynamical systems*, J.C. Martin, N.G. Markley and W. Perrizo (eds.), *Lecture Notes in Mathematics*, vol. 668, pp. 48–66. Springer (1978)
10. Franceschini, V.: Bifurcations of tori and phase locking in a dissipative system of differential equations. Physica D **6**, 285–304 (1983)
11. Gambaudo, J.M., Glendinning, P., Tresser, C.: Stable cycles with complicated structure. In: *Instabilities and nonequilibrium structures*, E. Tirapegui and D. Villarroel (eds.), *Mathematics and its Applications*, pp. 41–62. Reidel (1987)

12. Gaspard, P.: Measurement of the instability rate of a far-from-equilibrium steady state at an infinite period bifurcation. J. Phys. Chem. **94**(1), 1–3 (1990)
13. Giberti, C., Zanasi, R.: Behavior of a three-torus in truncated Navier–Stokes equations. Physica D **65**, 300–312 (1993)
14. Glazier, J.A., Libchaber, A.: Quasi-periodicity and dynamical systems: An experimentalist's view. IEEE Trans. Circuits and Systems **35**, 790–809 (1988)
15. Golubitsky, M., Schaeffer, D.G.: *Singularities and Groups in Bifurcation Theory.* Volume I. Springer (1985)
16. Golubitsky, M., Stewart, I., Schaeffer, D.G.: *Singularities and Groups in Bifurcation Theory.* Volume II. Springer (1988)
17. Kuznetsov, Y.A.: *Elements of Applied Bifurcation Theory, 2nd edn*. Springer (1998)
18. Lopez, J.M., Marques, F.: Dynamics of 3-tori in a periodically forced Navier–Stokes flow. Phys. Rev. Lett. **85**, 972–975 (2000)
19. Lopez, J.M., Marques, F., Sanchez, J.: Oscillatory modes in an enclosed swirling flow. J. Fluid Mech. **439**, 109–129 (2001)
20. Lopez, J.M., Marques, F., Shen, J.: An efficient spectral-projection method for the Navier–Stokes equations in cylindrical geometries II. three dimensional cases. J. Comput. Phys. **176**, 384–401 (2002)
21. Lopez, J.M., Shen, J.: An efficient spectral-projection method for the Navier–Stokes equations in cylindrical geometries I. Axisymmetric cases. J. Comput. Phys. **139**, 308–326 (1998)
22. Marques, F., Lopez, J.M., Iranzo, V.: Imperfect gluing bifurcation in a temporal glide-reflection symmetric Taylor–Couette flow. Phys. Fluids **14**, L33–L36 (2002)
23. Marques, F., Lopez, J.M., Shen, J.: A periodically forced flow displaying symmetry breaking via a three-tori gluing bifurcation and two-tori resonances. Physica D **156**, 81–97 (2001)
24. Mullin, T.: Disordered fluid motion in a small closed system. Physica D **62**, 192–201 (1993)
25. Mullin, T., Cliffe, K.A.: Symmetry breaking and the onset of time dependence in fluid mechanical systems. In: *Nonlinear Phenomena and Chaos*, S. Sarkar (ed.), pp. 96–112. Adam Hilger (1986)
26. von Stamm, J., Buzug, T., Pfister, G.: Frequency locking in axisymmetric Taylor–Couette flow. Phys. Lett. A **194**, 173–178 (1994)
27. von Stamm, J., Gerdts, U., Buzug, T., Pfister, G.: Symmetry breaking and period doubling on a torus in the VLF regime in Taylor–Couette flow. Phys. Rev. E **54**, 4938–4957 (1996)
28. Turaev, D.V.: Bifurcations of two-dimensional dynamical systems close to a system with two separatrix loops. Russian Math. Surveys **40**, 243–244 (1985)
29. Turaev, D.V., Shil'nikov, L.P.: On bifurcations of a homoclinic "figure eight" for a sadddle with a negative saddle value. Soviet Math. Dokl. **34**, 397–401 (1987)
30. Wittenberg, R.W., Holmes, P.: The limited effectiveness of normal forms: A critical review and extension of local bifurcation studies of the Brusselator PDE. Physica D **100**, 1–40 (1997)